

LETTER • OPEN ACCESS

Optical properties of two-dimensional tin nanosheets epitaxially grown on graphene

To cite this article: Eleonora Bonaventura *et al* 2024 *Nanotechnology* **35** 23LT01

View the [article online](#) for updates and enhancements.

You may also like

- [Titanium Nitride Nanoparticle Electrocatalysts for Oxygen Reduction Reaction in Alkaline Solution](#)
Ryohji Ohnishi, Masao Katayama, Dongkyu Cha *et al.*
- [Enhanced Performance of Li-O₂ Batteries with MoS₂ Nanosheet-Coated TiN Nanorods Arrays Grown on Carbon Paper As Binder-Free Cathodes](#)
Limin Leng and Shijun Liao
- [\(Invited\) Harvesting Sunlight Using Titanium Nitride Nanostructures for Enhanced Visible Photocatalytic Activity and Solar Heating](#)
Satoshi Ishii, Satish Laxman Shinde, Manpreet Kaur *et al.*

PRIME
PACIFIC RIM MEETING
ON ELECTROCHEMICAL
AND SOLID STATE SCIENCE

HONOLULU, HI
Oct 6–11, 2024


Abstract submission deadline:
April 12, 2024

Learn more and submit!

Joint Meeting of
The Electrochemical Society
•
The Electrochemical Society of Japan
•
Korea Electrochemical Society

Letter

Optical properties of two-dimensional tin nanosheets epitaxially grown on graphene

Eleonora Bonaventura^{1,2} , Christian Martella¹ , Salvatore Macis³,
Daya S Dhungana¹, Simonas Krotkus⁴, Michael Heuken⁴, Stefano Lupi^{3,5},
Alessandro Molle^{1,*}  and Carlo Grazianetti^{1,*} 

¹ CNR-IMM Unit of Agrate Brianza, via C. Olivetti 2, Agrate Brianza, Italy

² Department of Materials Science, University of Milano-Bicocca, via R. Cozzi 55, Milano, Italy

³ Department of Physics, Sapienza University, Piazzale Aldo Moro 5, Roma, Italy

⁴ AIXTRON SE, Herzogenrath, Germany

⁵ CNR-IOM, Q2 Building, Area Science Park, Basovizza-Trieste, Italy

E-mail: alessandro.molle@cnr.it and carlo.grazianetti@cnr.it

Received 4 December 2023, revised 23 February 2024

Accepted for publication 10 March 2024

Published 21 March 2024



CrossMark

Abstract

Heterostacks formed by combining two-dimensional materials show novel properties which are of great interest for new applications in electronics, photonics and even twistrionics, the new emerging field born after the outstanding discoveries on twisted graphene. Here, we report the direct growth of tin nanosheets at the two-dimensional limit via molecular beam epitaxy on chemical vapor deposited graphene on Al₂O₃(0001). The mutual interaction between the tin nanosheets and graphene is evidenced by structural and chemical investigations. On the one hand, Raman spectroscopy indicates that graphene undergoes compressive strain after the tin growth, while no charge transfer is observed. On the other hand, chemical analysis shows that tin nanosheets interaction with sapphire is mediated by graphene avoiding the tin oxidation occurring in the direct growth on this substrate. Remarkably, optical measurements show that the absorption of tin nanosheets exhibits a graphene-like behavior with a strong absorption in the ultraviolet photon energy range, therein resulting in a different optical response compared to tin nanosheets on bare sapphire. The optical properties of ultra-thin tin films therefore represent an open and flexible playground for the absorption of light in a broad range of the electromagnetic spectrum and technologically relevant applications for photon harvesting and sensors.

Supplementary material for this article is available [online](#)

Keywords: stanene, graphene, 2D heterostructures, xenes, molecular beam epitaxy, optical properties

1. Introduction

The rise of two-dimensional vertical heterostructures is currently reshaping the frontiers of new materials research [1–3]. The advantages of assembling different layers include not only an increase in possible functionalities, but also a higher stability of the individual heterostructure components and Xenes, the post-graphene synthetic lattices, are not excluded from this promising perspective [4, 5]. The first reported

* Authors to whom any correspondence should be addressed.

examples are of environmentally stable Xenes, such as phosphorene, mechanically exfoliated and stacked with other two-dimensional materials [6, 7]. Recently, the use of stanene as a template for the epitaxial growth of silicene (and vice versa) has proven to be a viable route for the realization of Xene-based heterostructures [8]. Moreover, the addition of a layer of stanene has been shown to weaken the interaction between the silicene and its native Ag substrate, making the properties of such decoupled silicene more accessible [9]. Epitaxial growth methods allow for the fabrication of heterostructures on a large scale, overcoming the limitations of mechanically assembled van der Waals flakes, whose lateral dimensions do not exceed tens of micrometers [10]. Despite these advances, metallic substrates severely limit the Xenes device integration, and this makes insulators particularly attractive for electronic and photonic applications [11–13].

The use of *c*-plane sapphire or Al₂O₃(0001) as a template is a suitable choice for the synthesis of Xenes. DFT calculations showed how Al₂O₃(0001), with its hexagonal surface symmetry, can stabilize the two-dimensional structure of silicon, germanium, and tin without affecting their electronic properties [14, 15]. Dirac-type electrostatics was then observed on epitaxially grown silicon nanosheets, following the low-energy behavior of the optical conductivity [16, 17]. The optical properties of tin nanosheets, grown directly on Al₂O₃(0001) by molecular beam epitaxy (MBE), showed stanene-like optical features when compared to calculated absorption spectra of freestanding stanene [17–19]. These stanene-like features deduced from optical spectroscopy were observed even if the chemical analysis carried out by x-ray photoelectron spectroscopy (XPS) demonstrated that tin undergoes a partial oxidation [17]. The formation of tin oxide has been explained by the unavoidable interaction between tin and the adsorbed hydroxyl group (–OH) on the surface of the Al₂O₃(0001) substrate [20, 21]. Engineering the substrate for the Xenes growth therefore has a twofold purpose. First, given the intrinsic metastable nature of Xenes, it is crucial to control the interaction between the material of interest and the supporting substrate. Second, from a general perspective, stacking different two-dimensional materials offers a great potential for tailoring the physical and chemical properties of each constituent or the whole coupled system [22, 23].

Graphene on Al₂O₃(0001) is a technologically relevant configuration that has attracted considerable interest in recent years [24–26]. The reduction of metal contamination, unintentional doping and mechanical stress are some of the benefits of using sapphire as a target substrate. In addition, the atomically planar graphene surface can act as a template to stabilize the growth of various two-dimensional materials [27, 28]. Few works show the direct synthesis of Xenes on graphene to obtain vertical heterostacks, for example silicene [29–31]. Instead, the possibility of growing stanene on graphene has been explored in different theoretical works [32, 33], while its experimental realization has recently been reported on Cu(111), achieving a uniform thickness, continuous morphology, and higher stability [34].

Here, we report on the use of graphene on Al₂O₃(0001) as a template for the epitaxial growth of tin nanosheets at the

two-dimensional limit. The structural properties of the heterostructure were investigated by Raman spectroscopy while optical spectroscopy was then used to measure the optical response of the tin nanosheets in the photon energy range from 0.3 to 6.5 eV (NIR-UV spectral range). The outcome is an open playground where the optical properties of the whole system can be easily modified, allowing versatile tuning of light absorption, especially when these findings are compared with the case without graphene in between tin nanosheets and the Al₂O₃(0001) substrate.

2. Methods

High-quality single-layer graphene was grown on single side polished Al₂O₃(0001) by chemical vapor deposition (CVD) in an AIXTRON CCS reactor, following the growth procedure described in [24, 35]. The sapphire substrate (Silian) had a nominal offcut angle of 0.25° towards the *m*-plane. Graphene on Al₂O₃(0001) (hereafter Gr-Al₂O₃) was then used as substrate for the tin nanosheets deposition. The 2 inch original wafer has been cut into $\sim 1 \times 1$ cm² pieces by a cleaving tool (LatticeGear). After the cut, graphene layers quality was evaluated via Raman spectroscopy and atomic force microscopy (AFM) analysis. Tin deposition on graphene was performed by MBE, in ultrahigh vacuum environment (base pressure 10^{−10} mbar), on degassed substrates using a *k*-cell evaporator for which the flux rate was previously calibrated through a quartz micro-balance. Tin was deposited at a deposition rate of 0.2 Å min^{−1}. Two tin thicknesses were considered, 0.5 and 1 nm, and were grown at room temperature. Both types of samples were then capped by an amorphous aluminum oxide capping layer (~ 5 nm) in order to prevent their degradation in ambient conditions [36]. The overall stacking is thus (from top to bottom) a-Al₂O₃/Sn/Gr/Al₂O₃(0001). Chemical properties of the samples were investigated *in situ* by means of XPS, monitoring the status of graphene and tin films at all stages of the growth. Non-monochromatized Mg K_α x-ray source was used to investigate the C 1s and Sn 3d_{5/2} core levels. Raman spectroscopy was used to assess quality, doping and strain of graphene before and after the tin deposition. Raman maps over areas of 7 × 7 μm² were acquired in backscattering configuration using a Renishaw InVia spectrometer equipped with 514 nm laser and 50 × (N. A. 0.75) objective. The incident laser power was kept below 3 mW to avoid heating effects and sample damages. The optical characterization was performed in the NIR-UV spectral range. The transmittance was measured at room temperature using a Cary 5000 spectrophotometer, covering the energy range between 0.3 and 6.5 eV. Oxygen plasma etching was used to remove graphene from the sapphire surface to provide a good reference for optical characterization. The optical conductivity of thin tin films was extracted through ReFIT by implementing a multilayer model [37]. Specifically, the transmittance of the samples, including the substrate, was fitted by using a double (Gr-Al₂O₃) or a three (Sn-Gr-Al₂O₃) layers Kramers-Kronig consistent Drude–Lorentz model.

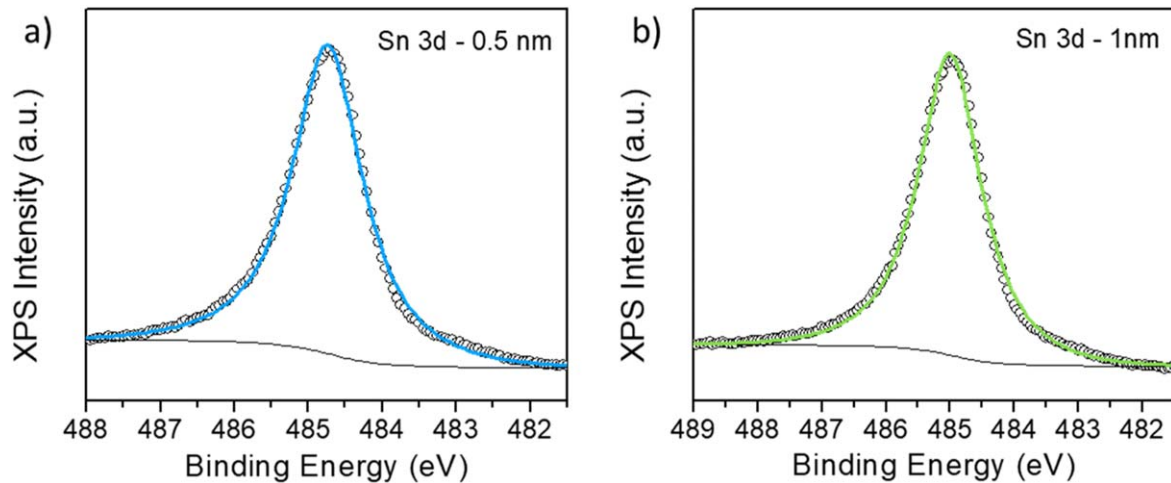


Figure 1. (a)–(b) XPS spectra of the Sn $3d_{5/2}$ core level of 0.5 (blue) and 1 (green) nm tin grown at RT on Gr- Al_2O_3 showing a single component related to the elemental states of Sn. Open circles represent the raw data.

3. Results and discussion

To determine the properties of tin in the two-dimensional limit, we studied samples of different thicknesses grown on Gr- Al_2O_3 substrates. Two different tin thicknesses, 0.5 and 1 nm, were considered in the following. *In situ* XPS was carried out to check the chemical status of the tin films after the growth. The Sn $3d_{5/2}$ core level, for the 0.5 nm thick sample, is reported in figure 1(a). The spectrum shows the core level related to the elemental tin placed at binding energy (BE) of 484.7 eV with a full-width half maximum (FWHM) of 1.15 eV. When the tin thickness is increased to 1 nm, the Sn $3d_{5/2}$ core level in figure 1(b) is still characterized by a single component at the same BE. The absence of any oxide-related component indicates that graphene is effective in avoiding the chemical interaction between the tin nanosheets and the $\text{Al}_2\text{O}_3(0001)$ substrate. The comparison between the Sn $3d_{5/2}$ core level of 0.5 nm tin films grown directly on $\text{Al}_2\text{O}_3(0001)$ and on the graphene buffer layer is shown in figure A.1 of the Supplementary Information (SI). Furthermore, the lack of additional components in the Sn $3d_{5/2}$ core level spectrum suggests that the chemical interaction between tin and graphene is low, as also confirmed by the C 1s spectra reported in figure A.2 of SI. Figure A.2 shows that the C 1s core level is made of two components, one related to sp^2 carbon (graphene) and the other to C–H bonding [25]. After tin deposition, the graphene-related component of the C 1s XPS spectrum undergoes a negligible BE shift (+0.11 and –0.11 eV, for 0.5 and 1 nm, respectively), thus making evidence of limited chemical interaction between the tin nanosheets and the underlying graphene. After the tin nanosheets deposition, the samples were capped with a 5 nm thick amorphous Al_2O_3 layer grown *in situ* by MBE to prevent oxidation in ambient conditions and to allow for Raman and optical spectroscopy investigations (see Methods) [36].

Tin exhibits active Raman modes for wavenumbers below 300 cm^{-1} in both its bulk and two-dimensional forms [38–40]. Raman characterization of the tin nanosheets, in the $100\text{--}400\text{ cm}^{-1}$ spectral range, revealed no peaks associated

with tin as already observed for the case without graphene because of the low Raman scattering cross-section of tin in this nanoscale regime [17]. However, unlike direct growth on $\text{Al}_2\text{O}_3(0001)$, the graphene buffer layer allows us to infer how the presence of the tin nanosheets affects the underlying graphene by modifying its well-known Raman modes [41]. Indeed, by evaluating the effects of the tin deposition on the Raman response of graphene, it was possible to gain information about the properties of the whole heterostructure. In fact, as a first approximation, for a single layer of graphene, any shift or line widening of the G and 2D Raman modes can be related to strain and/or doping effects [42]. The Raman spectrum of graphene on $\text{Al}_2\text{O}_3(0001)$ obtained from a single-point acquisition is shown in figure A.3a in SI where the fingerprints of the electron–phonon interaction in a single layer graphene are disclosed. The statistical analysis, carried out on Raman maps acquired over several areas of $7 \times 7\ \mu\text{m}^2$, results in the G band located at $1588 \pm 1\text{ cm}^{-1}$ with a FWHM of $18 \pm 3\text{ cm}^{-1}$ and the 2D band at $2690 \pm 2\text{ cm}^{-1}$ with the FWHM of $39 \pm 4\text{ cm}^{-1}$. These values are in agreement with those measured for graphene directly grown on $\text{Al}_2\text{O}_3(0001)$ and reported in works using a similar statistical approach [24, 35, 43]. Moreover, the values of the 2D/G intensity ratio 2.5 ± 0.2 indicate a low charge carrier concentration [44]. According to the calibration curve reported by Das *et al* [44] we estimate a carrier concentration of $\sim 1.5 \times 10^{12}\text{ cm}^{-2}$. Table A.1 in SI reports the values obtained from the statistical analysis performed on the three areas of the wafer highlighted (green squares) in figure A.3b. The surface morphology of graphene on $\text{Al}_2\text{O}_3(0001)$ in figure A.3c, obtained by aAFM, shows a high density of wrinkles on the slabs surface with a typical height of 1–2 nm. Such structures are consequence of the mismatch between the thermal expansion coefficient of graphene and sapphire as reported in literature [24, 25]. With the graphene modes kept as reference, we investigated the evolution of the Raman spectrum of graphene with increasing thickness of the tin nanosheets (figure 2(a)).

With respect to the Raman modes of the pristine graphene, after the tin deposition we observed the broadening of

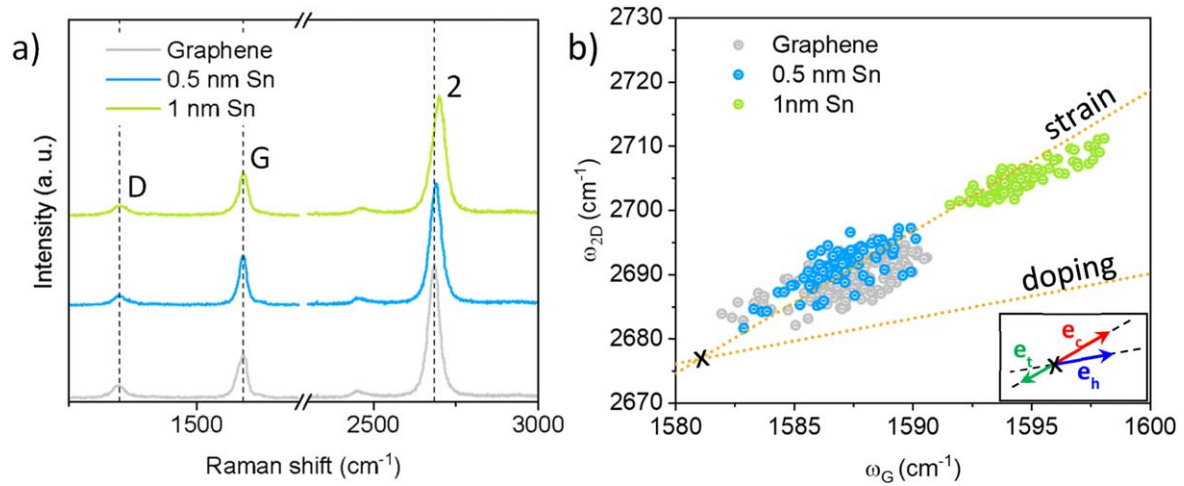


Figure 2. (a) Raman spectra of graphene before (gray) and after the growth of tin nanosheets 0.5 nm (blue) and 1 nm (green) thick. (b) Correlation plot between the frequencies of the G and the 2D modes of graphene (ω_G , ω_{2D}) measured on pristine graphene and after the growth of tin nanosheets, 0.5 nm (blue) and 1 nm (green) thick. The ‘strain’ orange line describes neutral-charge graphene under compressive strain. The ‘doping’ orange line indicates p-type doped graphene. In the inset, the arrows labeled e_t , e_c and e_h represent the trajectories of $(\omega_G^0, \omega_{2D}^0)$ affected by tensile strain, compressive strain and hole doping, respectively.

the 2D mode and the blue-shift of both G and 2D modes. Specifically, the FWHM of the 2D peak in the spectra reported in figure 2(a) increases with the thickness of the deposited tin, going from 39 to 42 cm^{-1} for 0.5 and 1 nm thick nanosheets, respectively. The 2D/G peaks intensity ratio, despite a slight increase to 2.7 ± 0.2 , is compatible with the value obtained for bare graphene and with a negligible (or low) charge carrier transfer (i.e. doping. See also discussion below) from both 0.5 and 1 nm deposited tin [44]. Moreover, the D peak is still visible without any significant variation, suggesting that the homogeneity of graphene has not been affected by the growth.

As mentioned above, Raman spectroscopy is a very helpful method for extracting information about the doping and strain to which graphene is subjected. An inverse approach was therefore used to shed light on the interaction between tin and graphene in the stacked configuration. We exploited the variation of the Raman response of graphene, induced by the deposition of tin films with different thicknesses, with the aim of gaining information on the resulting heterostructure. The correlation plot of the Raman shifts of the G and 2D peaks, shown in figure 2(b), allows us to separate the contribution of doping and strain [42]. The directions along which the pure compressive strain-induced and pure hole doping-induced shifts are expected are indicated by the two dashed orange lines. Moreover, the point where the two lines intersect, located at $(\omega_G^0, \omega_{2D}^0) = (1582, 2677)$, identifies graphene not affected by strain or excess charges [42]. It is worth noting that from a more general perspective there are three directions that the data can follow, which are represented by the colored vectors in the inset of figure 2(b): the e_c (e_c) vector describes the effect of compressive (tensile) strain, while hole doping follows the e_h direction. The introduction of this reference system divides the ω_G - ω_{2D} space into four regions (three of which are visible in figure 2(b)). The Raman peak positions of graphene under

strain or doping will move from the intrinsic value of strain-free and charge-neutral graphene. Thus, the estimation of strain and doping levels from the experimental data is performed by projecting the center of gravity of each data set onto the strain and doping axes. Using reference values corresponding to the shifts obtained, the magnitude of strain and doping can then be calculated [42, 45, 46]. The correlation map shows that graphene on the $\text{Al}_2\text{O}_3(0001)$ substrate is strained prior to tin deposition. This effect can be due to the interaction between graphene and sapphire, which results in the formation of wrinkles. No substantial differences are observed between the uncovered graphene and after the deposition of the 0.5 nm thick tin nanosheet. Conversely, when tin nanosheets thickness increases, the dispersion shows that graphene undergoes a compressive strain while the effect on charge doping is negligible. Assuming a uniaxial strain-sensitivity of the G mode $\Delta\omega_G/\Delta\varepsilon = -23.5 \text{ cm}^{-1}/\%$ the corresponding compressive strain due to the 1 nm thick nanosheet deposition is about 0.5% [42, 47]. Interestingly, the type of stress to which graphene is subjected can provide information about the possible intercalation of tin atoms. It has recently been reported that, under certain temperature and impurity conditions, silicene grown on graphene can exhibit intercalation [48]. In this case, the Raman spectrum of graphene shows a splitting of the G peak and the 2D peak downshift, both aspects being indicative of the tensile strain experienced by graphene [49]. The different Raman response and the compressive strain that the graphene is subjected to, after the deposition of the tin nanosheets, suggest that intercalation effects can be ruled out. Moreover, it is important to stress that the effects of such as desorption and intercalation typically occur during high-temperature growth or post-growth annealing, whereas all the samples scrutinized here were grown at room temperature.

The optical response of the heterostructures formed by the tin nanosheets and graphene on $\text{Al}_2\text{O}_3(0001)$ has been

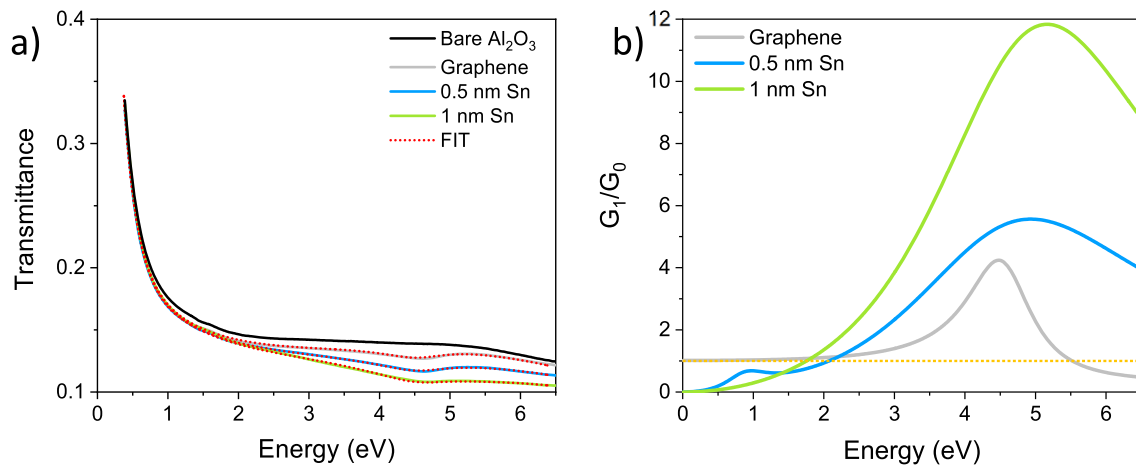


Figure 3. (a) Transmittance of supported graphene (gray), 0.5 nm (blue) and 1 nm (green) thick tin nanosheets. The bare Al₂O₃(0001) transmittance (black line) is reported as reference. (b) Normalized optical conductance of graphene (gray), 0.5 nm (blue) and 1 nm (green) thick tin nanosheets, extracted from multi-layer models.

investigated by NIR-UV spectroscopy. Figure 3(a) shows the absolute transmittance for the two tin samples, together with those for Gr-Al₂O₃ and the bare Al₂O₃(0001), in the photon energy range between 0.3 and 6.5 eV. As expected, the observed decrease of transmittance in the spectra of figure 3(a) is consistent with an increase in absorption in the thicker tin film. The optical conductivity of graphene, 0.5 and 1 nm thick tin nanosheets was obtained by fitting (red-dashed line in figure 3(a)) the transmittance spectra by means of the RefFIT software (see Methods) [37]. In the spectral analysis, the thickness of the nanosheets was left as a free parameter. The best fit to the experimental data was obtained for the values shown in table A.2 in SI, which also correspond to the nominal values. The extracted real part of the optical conductivity $\sigma_1(\omega)$ was used to calculate the normalized optical conductance $G_1/G_0 = \sigma_1(\omega)d/G_0$ reported in figure 3(b), where d is the thickness of the considered layer and $G_0 = e^2/4\hbar$ is the universal conductance [50, 51]. The optical conductance can be used for a fair comparison between samples of different thicknesses. $G_1(\omega)$ for graphene shows the typical behavior described by the superposition of a nearly flat background in the whole IR range (0.3–1.5 eV) due to the intraband transitions, and an asymmetric absorption peak at ~4.6 eV [52]. This feature is related, in the independent-particle description, to the interband transitions from the bonding to the antibonding π states near the saddle-point singularity at the M point of Brillouin zone [53]. At the lowest thickness of tin, $G_1(\omega)$ shows a small absorption peak around 0.9 eV, without the flat background, and rises around 1.5 eV up to the UV range (blue curve in figure 3(b)). The maximum value occurs at ~5 eV shifted and broadened with respect to graphene absorption. When the tin nanosheet thickness increases to 1 nm, the absorption peak in the IR region disappears and the rise becomes steeper with a small shift of the $G_1(\omega)$ maximum to further higher energies. Surprisingly, both tin nanosheets exhibit an enhanced optical absorption compared to graphene, starting at ~2 eV, as expected for stanene in the stanene-graphene heterostructure [33]. It should be emphasized that the real part of the optical conductivity, and

therefore the conductance, shown in figure 3(b), is related to the individual tin layers. In the applied multilayer model, the contribution of graphene and substrate can be considered separately, allowing the optical response of the tin nanosheets to be extracted from the overall optical response of the whole system. For the sake of completeness, the latter one is shown in figure A.4 in SI. As the thickness of the tin layer increases, the optical contribution of graphene to the shape of the overall system response decreases, making the optical response of the combined tin nanosheets-graphene system strongly tin-like.

As already shown for the direct deposition on Al₂O₃(0001) [17], the optical behavior of the tin nanosheets is unusual even with the graphene buffer layer. This aspect is supported by the comparisons between the normalized optical absorbance $A(\omega)$ of different tin-based structures, shown in figure 4. The absorbance was calculated from the imaginary part of the refractive index $\tilde{n}(\omega) = n(\omega) + i\kappa(\omega)$ as $A(\omega) = 2\kappa(\omega)\omega d$, where $\alpha(\omega) = 2\kappa(\omega)\omega$ is the absorption coefficient of the material. The absorption spectra of the 0.5 and 1 nm thick tin nanosheets reported in figure 4(a) deviate from those of the two allotropic forms of tin, the α - and β -Sn [54, 55]. At low frequencies, however, their $A(\omega)$ approaches zero similar to α -Sn. In this context, it is worth noting that the epitaxy on lattice-matched substrates has been reported as a possible strategy for stabilizing the α -Sn at room temperature [38, 56]. Moreover, it is important to stress that the poor correspondence between the optical response of the tin nanosheets and the α -Sn might be attributed to the small thickness of the nanosheets compared to the reference (128 nm) [54]. Figure 4(b) shows the comparison between $A(\omega)$ of the tin nanosheets and the calculated absorbance of free-standing stanene reported in [18, 19]. The spectrum calculated by John *et al* [19] shows low- and high-energy features that match with the experimental data for the broad peaks at ~1 and ~5 eV. Finally, figure 4(c) shows the absorption spectrum of the 0.5 nm thick tin nanosheet grown on Gr-Al₂O₃ and that of a tin nanosheet of the same thickness directly grown on the Al₂O₃ substrate [17]. The spectra in figure 4(c) are qualified by a shift of the absorption maximum towards higher photon

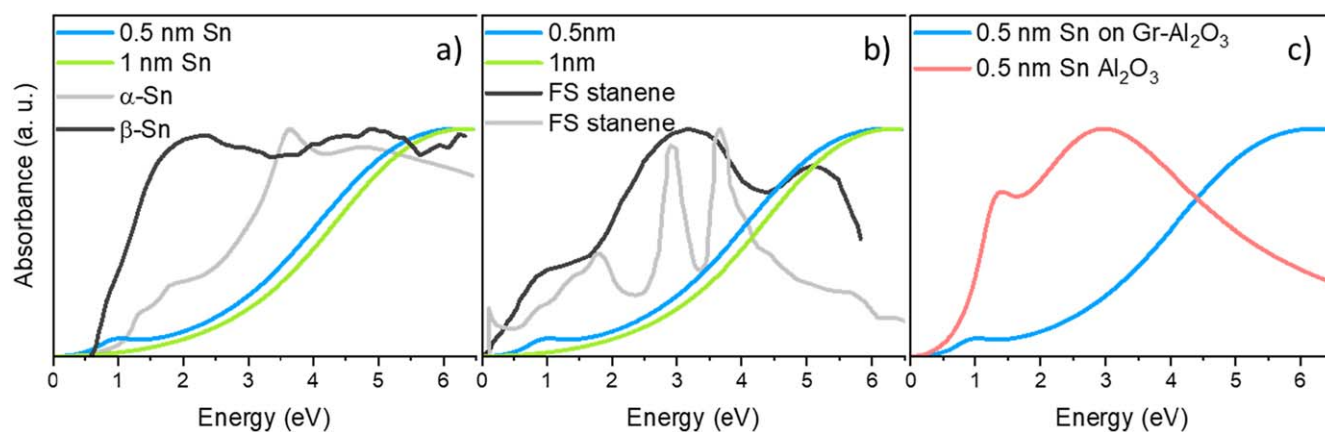


Figure 4. (a) Absorption spectra of 0.5 nm (blue) and 1 nm thick (green) tin nanosheets and those of α -Sn (gray) and β -Sn (black) (data from [54, 55]). (b) Absorbance of 0.5 nm (blue) and 1 nm thick (green) tin nanosheets compared with the absorbance of freestanding stanene reported in [18] (gray) and [19] (black). (c) Absorbance of 0.5 nm thick tin nanosheet grown on Gr- Al_2O_3 (blue) and 0.5 nm thick tin nanosheet grown directly on Al_2O_3 (red) reported in [17].

energy when tin is grown on a buffer layer of graphene. The Lorentzian oscillator used to model this absorption moves from 2.8 to 4.9 eV in the presence of graphene. Similarly, the second Lorentzian contribution, which is used to model the absorption at lower energies, shifts down from 1.3 eV for direct tin growth to 0.9 eV with graphene. We can thus conclude that the interlayer coupling plays a crucial role in modifying the optical properties of a hybrid system. The optical response of the tin nanosheets supported by $\text{Al}_2\text{O}_3(0001)$ or Gr- $\text{Al}_2\text{O}_3(0001)$ can be tuned over a wide range of photon energies covering the VIS and the UV spectrum. Such a tunability of the optical conductivity can be achieved by differently assembling the elements of the heterostructure stacking.

4. Conclusions

The successful growth of tin nanosheets at two-dimensional limit has been reported on the Gr- $\text{Al}_2\text{O}_3(0001)$ template. At variance with the direct growth on $\text{Al}_2\text{O}_3(0001)$, inserting a graphene buffer layer in between turns out to minimize the chemical interaction with the substrate and then the oxidized component. The structural characterization by Raman spectroscopy demonstrated that graphene after tin deposition is affected by a tin thickness-dependent compressive strain but not by charge transfer effects i.e. doping. The strain can be related to the interaction with tin overlayer which, however, shows no signs of intercalation or chemical bonding between tin and carbon. Interestingly, the role of graphene is not limited to the prevention of tin oxidation, but also enables the optical engineering of the tin nanosheets. Optical measurements in the NIR-UV spectral range identify an increased absorption starting from 2 eV towards higher energies, as expected from theoretical calculations performed on stanene-graphene heterostructure. More importantly, similarities were observed in the optical response of the tin nanosheets and the semi-metallic allotropic form of tin, suggesting the possibility of stabilizing α -Sn on Gr- $\text{Al}_2\text{O}_3(0001)$ at room temperature. By comparing

the optical properties of graphene and tin nanosheets, with and without a graphene buffer layer, our findings provide a promising route to modulate light absorption by active two-dimensional layers in the VIS and UV photon range, setting the scene for ultra-scaled photonic devices.

Acknowledgments

The authors thank Mario Alia (CNR-IMM) for technical assistance, Sara Ghomi (CNR-IMM) for AFM analysis and Alessio Lamperti (CNR-IMM) for fruitful discussions.

Data availability statement

All data that support the findings of this study are included within the article (and any supplementary files).

CRediT author statement

Eleonora Bonaventura: Investigation, Methodology, Formal analysis, Data Curation, Writing—Original Draft, Visualization. **Christian Martella:** Conceptualization, Methodology, Writing—Review and Editing, Supervision. **Salvatore Macis:** Formal analysis, Writing—Review and Editing. **Daya S Dhungana:** Investigation, Writing—Review and Editing. **Simonas Krotkus:** Investigation. **Michael Heuken:** Investigation. **Stefano Lupi:** Writing—Review and Editing, Funding acquisition. **Alessandro Molle:** Conceptualization, Writing—Review and Editing, Supervision, Project administration, Funding acquisition. **Carlo Grazianetti:** Conceptualization, Methodology, Investigation, Writing—Review and Editing, Supervision.

Funding

This research was funded by European Commission within the H2020 research and innovation program under the

ERC-COG 2017 Grant No. 772261 'XFab' and partially supported by the Italian Ministry of University and Research (MUR) under the PRIN 2020 Grant No. 2020RPEPNH 'PHOTO'.

ORCID iDs

Eleonora Bonaventura  <https://orcid.org/0000-0002-1561-8474>

Christian Martella  <https://orcid.org/0000-0003-1811-165X>

Alessandro Molle  <https://orcid.org/0000-0002-3860-4120>

Carlo Grazianetti  <https://orcid.org/0000-0003-0060-9804>

References

- [1] Wang Y *et al* 2022 A gate-tunable artificial synapse based on vertically assembled van der Waals ferroelectric heterojunction *J. Mater. Sci. Technol.* **128** 239–44
- [2] Ye Q, Lu J, Yi H, Zheng Z, Ma C, Du C, Zou Y, Yao J and Yang G 2022 A flexibly switchable TaIrTe₄-WSe₂ van der Waals heterojunction photodetector with linear-polarization-dependent photosensitivity *Appl. Phys. Lett.* **120** 181104
- [3] Rebolledo Espinoza C, Ryndyk D A, Dianat A, Gutierrez R and Cuniberti G 2022 First principles study of field effect device through van der Waals and lateral heterostructures of graphene, phosphorene and graphane *Nano Mater. Sci.* **4** 52–9
- [4] Liu Y, Weiss N O, Duan X, Cheng H-C, Huang Y and Duan X 2016 Van der Waals heterostructures and devices *Nat. Rev. Mater.* **1** 16042
- [5] Grazianetti C and Molle A 2022 Xene heterostructures *Xenes* (Elsevier) pp 377–403
- [6] Deng Y, Luo Z, Conrad N J, Liu H, Gong Y, Najmaei S, Ajayan P M, Lou J, Xu X and Ye P D 2014 Black phosphorus-monolayer MoS₂ van der Waals heterojunction p–n diode *ACS Nano* **8** 8292–9
- [7] Chen X *et al* 2015 High-quality sandwiched black phosphorus heterostructure and its quantum oscillations *Nat. Commun.* **6** 7315
- [8] Dhungana D S, Grazianetti C, Martella C, Achilli S, Fratesi G and Molle A 2021 Two-dimensional silicene–stanene heterostructures by epitaxy *Adv. Funct. Mater.* **31** 2102797
- [9] Bonaventura E, Dhungana D S, Martella C, Grazianetti C, Macis S, Lupi S, Bonera E and Molle A 2022 Optical and thermal responses of silicene in xene heterostructures *Nanoscale Horiz.* **7** 924–30
- [10] Castellanos-Gomez A, Buscema M, Molenaar R, Singh V, Janssen L, van der Zant H S J and Steele G A 2014 Deterministic transfer of two-dimensional materials by all-dry viscoelastic stamping *2D Mater.* **1** 011002
- [11] Johnson R A, de la Houssaye P R, Chang C E, Pin-Fan Chen, Wood M E, Garcia G A, Lagnado I and Asbeck P M 1998 Advanced thin-film silicon-on-sapphire technology: microwave circuit applications *IEEE Trans. Electron Devices* **45** 1047–54
- [12] Baehr-Jones T, Spott A, Ilic R, Spott A, Penkov B, Asher W and Hochberg M 2010 Silicon-on-sapphire integrated waveguides for the mid-infrared *Opt. Express* **18** 12127
- [13] Chen Z *et al* 2019 Improved epitaxy of AlN film for deep-ultraviolet light-emitting diodes enabled by graphene *Adv. Mater.* **31** 1807345
- [14] Chen M X, Zhong Z and Weinert M 2016 Designing substrates for silicene and germanene: first-principles calculations *Phys. Rev. B* **94** 075409
- [15] Wang H, Pi S T, Kim J, Wang Z, Fu H H and Wu R Q 2016 Possibility of realizing quantum spin Hall effect at room temperature in stanene/Al₂O₃(0001) *Phys. Rev. B* **94** 035112
- [16] Grazianetti C, De Rosa S, Martella C, Targa P, Codegoni D, Gori P, Pulci O, Molle A and Lupi S 2018 Optical conductivity of two-dimensional silicon: evidence of dirac electrodynamics *Nano Lett.* **18** 7124–32
- [17] Grazianetti C, Bonaventura E, Martella C, Molle A and Lupi S 2021 Optical properties of stanene-like nanosheets on Al₂O₃ (0001): implications for xene photonics *ACS Appl. Nano Mater.* **4** 2351–6
- [18] Matthes L, Pulci O and Bechstedt F 2014 Optical properties of two-dimensional honeycomb crystals graphene, silicene, germanene, and tinene from first principles *New J. Phys.* **16** 105007
- [19] John R and Merlin B 2017 Optical properties of graphene, silicene, germanene, and stanene from IR to far UV—a first principles study *J. Phys. Chem. Solids* **110** 307–15
- [20] Ahn J and Rabalais J W 1997 Composition and structure of the Al₂O₃(0001)-(1 × 1) surface *Surf. Sci.* **388** 121–31
- [21] Niu C, Shepherd K, Martini D, Tong J, Kelber J A, Jennison D R and Bogicevic A 2000 Cu interactions with α-Al₂O₃(0001): effects of surface hydroxyl groups versus dehydroxylation by Ar-ion sputtering *Surf. Sci.* **465** 163–76
- [22] Pham P V, Bodepudi S C, Shehzad K, Liu Y, Xu Y, Yu B and Duan X 2022 2D Heterostructures for ubiquitous electronics and optoelectronics: principles, opportunities, and challenges *Chem. Rev.* **122** 6514–613
- [23] Li M-Y, Chen C-H, Shi Y and Li L-J 2016 Heterostructures based on two-dimensional layered materials and their potential applications *Mater. Today* **19** 322–35
- [24] Mishra N *et al* 2019 Wafer-scale synthesis of graphene on sapphire: toward fab-compatible graphene *Small* **15** 1904906
- [25] Chen Z *et al* 2021 Direct growth of wafer-scale highly oriented graphene on sapphire *Sci. Adv.* **7** 115
- [26] Li J *et al* 2022 Wafer-scale single-crystal monolayer graphene grown on sapphire substrate *Nat. Mater.* **21** 740–7
- [27] Hoang A T, Katiyar A K, Shin H, Mishra N, Forti S, Coletti C and Ahn J-H 2020 Epitaxial growth of wafer-scale molybdenum disulfide/graphene heterostructures by metal–organic vapor-phase epitaxy and their application in photodetectors *ACS Appl. Mater. Interfaces* **12** 44335–44
- [28] Piccinini G, Forti S, Martini L, Pezzini S, Miseikis V, Starke U, Fabbri F and Coletti C 2020 Deterministic direct growth of WS₂ on CVD graphene arrays *2D Mater.* **7** 014002
- [29] Sone J, Yamagami T, Nakatsuji K and Hirayama H 2016 Si growth at graphene surfaces on 6H-SiC(0001) substrates *Jpn. J. Appl. Phys.* **55** 035502
- [30] Li G *et al* 2018 Stable silicene in graphene/silicene van der waals heterostructures *Adv. Mater.* **30** 1804650
- [31] Ben Jabra Z *et al* 2022 Van der waals heteroepitaxy of air-stable quasi-free-standing silicene layers on CVD epitaxial graphene/6H-SiC *ACS Nano* **16** 5920–31
- [32] Wu L, Lu P, Bi J, Yang C, Song Y, Guan P and Wang S 2016 Structural and electronic properties of two-dimensional stanene and graphene heterostructure *Nanoscale Res. Lett.* **11** 525
- [33] Chen X, Meng R, Jiang J, Liang Q, Yang Q, Tan C, Sun X, Zhang S and Ren T 2016 Electronic structure and optical properties of graphene/stanene heterobilayer *Phys. Chem. Chem. Phys.* **18** 16302–9
- [34] Wu H, Tang J, Liang Q, Shi B, Niu Y, Si J, Liao Q and Dou W 2019 A van der Waals epitaxial growth of ultrathin two-dimensional Sn film on graphene covered Cu(111) substrate *Appl. Phys. Lett.* **115** 141601

- [35] Wördenweber H, Karthäuser S, Grundmann A, Wang Z, Aussen S, Kalisch H, Vescan A, Heuken M, Waser R and Hoffmann-Eifert S 2022 Atomically resolved electronic properties in single layer graphene on α -Al₂O₃(0001) by chemical vapor deposition *Sci. Rep.* **12** 18743
- [36] Molle A, Faraone G, Lamperti A, Chiappe D, Cinquanta E, Martella C, Bonera E, Scalise E and Grazianetti C 2021 Stability and universal encapsulation of epitaxial xenes *Faraday Discuss.* **227** 171–83
- [37] Kuzmenko A B 2005 Kramers–krönig constrained variational analysis of optical spectra *Rev. Sci. Instrum.* **76** 083108
- [38] Song H, Yao J, Ding Y, Gu Y, Deng Y, Lu M-H, Lu H and Chen Y-F 2019 Thermal stability enhancement in epitaxial alpha tin films by strain engineering *Adv. Eng. Mater.* **21** 1900410
- [39] Li M, Zheng L, Zhang M, Lin Y, Li L, Lu Y, Chang G, Klar P J and He Y 2019 From stannous oxide to stannic oxide epitaxial films grown by pulsed laser deposition with a metal tin target *Appl. Surf. Sci.* **466** 765–71
- [40] Zheng X, Zhang J-F, Tong B and Du R-R 2020 Epitaxial growth and electronic properties of few-layer stanene on InSb (1 1 1) *2D Mater.* **7** 011001
- [41] Ferrari A C and Basko D M 2013 Raman spectroscopy as a versatile tool for studying the properties of graphene *Nat. Nanotechnol.* **8** 235–46
- [42] Lee J E, Ahn G, Shim J, Lee Y S and Ryu S 2012 Optical separation of mechanical strain from charge doping in graphene *Nat. Commun.* **3** 1024
- [43] Song H J, Son M, Park C, Lim H, Levendorf M P, Tsen A W, Park J and Choi H C 2012 Large scale metal-free synthesis of graphene on sapphire and transfer-free device fabrication *Nanoscale* **4** 3050
- [44] Das A *et al* 2008 Monitoring dopants by Raman scattering in an electrochemically top-gated graphene transistor *Nat. Nanotechnol.* **3** 210–5
- [45] Ahn G, Kim H R, Ko T Y, Choi K, Watanabe K, Taniguchi T, Hong B H and Ryu S 2013 Optical probing of the electronic interaction between graphene and hexagonal boron nitride *ACS Nano* **7** 1533–41
- [46] Mueller N S *et al* 2017 Evaluating arbitrary strain configurations and doping in graphene with Raman spectroscopy *2D Mater.* **5** 015016
- [47] Yoon D, Son Y-W and Cheong H 2011 Strain-dependent splitting of the double-resonance Raman scattering band in graphene *Phys. Rev. Lett.* **106** 155502
- [48] Fabbri F *et al* 2022 Silicene nanosheets intercalated in slightly defective epitaxial graphene on a 4H-SiC(0001) substrate *Surf. Interfaces* **33** 102262
- [49] Mohiuddin T M G *et al* 2009 Uniaxial strain in graphene by Raman spectroscopy: G peak splitting, Gruneisen parameters, and sample orientation *Phys. Rev. B* **79** 205433
- [50] Kuzmenko A B, van Heumen E, Carbone F and van der Marel D 2008 Universal optical conductance of graphite *Phys. Rev. Lett.* **100** 117401
- [51] Perucchi A, Baldassarre L, Marini C, Postorino P, Bernardini F, Massidda S and Lupi S 2012 Universal conductivity and the electrodynamics of graphite at high pressures *Phys. Rev. B* **86** 035114
- [52] Mak K F, Sfeir M Y, Wu Y, Lui C H, Misewich J A and Heinz T F 2008 Measurement of the optical conductivity of graphene *Phys. Rev. Lett.* **101** 196405
- [53] Mak K F, Shan J and Heinz T F 2011 Seeing many-body effects in single- and few-layer graphene: observation of two-dimensional saddle-point excitons *Phys. Rev. Lett.* **106** 046401
- [54] Carrasco R A, Zamarripa C M, Zollner S, Menéndez J, Chastang S A, Duan J, Grzybowski G J, Clafin B B and Kiefer A M 2018 The direct bandgap of gray α -tin investigated by infrared ellipsometry *Appl. Phys. Lett.* **113** 232104
- [55] Takeuchi K and Adachi S 2009 Optical properties of β -Sn films *J. Appl. Phys.* **105** 073520
- [56] Dong X, Zhang L, Yoon M and Zhang P 2021 The role of substrate on stabilizing new phases of two-dimensional tin *2D Mater.* **8** 045003